

A centipede-inspired bonded-type ultrasonic actuator with high thrust force density driven by dual-torsional-vibration-induced flexural traveling waves

Jinshuo Liu^a, Longhui Ding^b, Chengqi Pan^c, Xiaohang Lai^a, Jiang Wu^{a,*}, Zhaochun Ding^a, Lipeng Wang^a, Xuhui Jing^b, Yili Wang^b, Leilei Lv^b, Xiaojaia Zhu^b, Xiaoming Yue^c

^a Center for Robotics, School of Control Science and Engineering, Shandong University, Jinan 250061, China

^b Goertek Inc., Weifang 261000, China

^c School of Mechanical Engineering, Shandong University, Jinan 250061, China



ARTICLE INFO

Keywords:

Ultrasonic actuator
Thrust force density
Torsional vibration
Flexural traveling wave

ABSTRACT

This paper presents an ultrasonic actuator with high thrust force density driven by dual-torsional-vibration-induced flexural traveling waves. Here, the PZT plates are bonded onto a duralumin vibrating body in a block shape to accomplish a compact configuration and they operate in the 2nd torsional vibrations, whose strong electromechanical coupling effect facilitates the enhancement of the driving force. Interestingly, the operating principle somewhat imitates the movement pattern of the centipede's feet. To test the validity, first, by using a Mason-equivalent-circuit-based dynamic model, several key dimensions were tuned to increase the driving-force-to-weight ratio. Meanwhile, the driving feet's configurations are adjusted based on a kinetic model to make the elliptical motion shape close to a circle. Then, an actuator prototype with the size of $48 \times 47 \times 6 \text{ mm}^3$ and the weight of 29 g was fabricated and the moving/loading/positioning performance was evaluated. When the actuator adopts a continuous operation, its maximal sliding speed reached 630 mm/s at the frequency of 24.95 kHz. Moreover, it yielded the maximal thrust force and the maximal output power of 4.38 N and 527.8 mW, corresponding to the thrust force density and the power density of 151.2 N/kg and 18.2 W/kg, respectively. In a stepping operation, the minimal step displacement was 0.91 μm . These results demonstrate that the dual-torsional-vibrations-induced traveling wave allows the actuator to produce the high thrust force density and provides a new actuating principle to design powerful ultrasonic actuators.

1. Introduction

Ultrasonic actuators (UAs) employ the inverse piezoelectric effect to convert the electrical energy into the mechanical vibration [1–3] and achieve the actuating function through the friction [4,5]. Owing to simple structures, self-locking at the power-off stage, and absence of electromagnetic interference [6,7], UAs have become potentially applicable to some special fields [8], e.g., optical system [9,10], miniature robots [11,12], or medical instruments [13,14]. To accelerate the practical application in these fields, it is essential to enhance UA's thrust force densities as they contribute to not only lightweight but also good controllability of entire system [15–17].

According to the lead-zirconate-titanate (PZT) plates' attaching method, UAs can be categorized as the clamped- and bonded-type ones [18–21]. By bolting the PZT plates with metal vibrating bodies, the clamped-type UAs generally have large mechanical outputs and stable

structures [22,23]. For example, Wang et al. [24] developed a bolt-clamped stepping actuator by exciting the longitudinal and bending vibrations to sequentially clamp and drive the slider, and the actuator had the speed and the maximal payload of respectively 0.72 mm/s and 1.47 kg. Deng et al. [25] designed the three-jaw type clamping mechanism to form an inchworm actuator with the maximal speed of 155.5 $\mu\text{m}/\text{s}$ and the maximal thrust force of 12.3 N. Liu et al.'s piezoelectric actuator [26], excited by single-phase and dual-phase excitation methods in an alternating way, provided the maximal speed and the maximal thrust force of respectively 483.7 mm/s and 3.4 N. In general, the clamped-type UAs have large thrust force dominantly because of high stiffness, but the usage of the clamping mechanism as well as the large-sized PZT plates makes it difficult to reduce the transducer's weight and consequently decrease the thrust force density [27]. As an alternative approach, the PZT plates (commonly in thick profiles) are bonded onto the metal vibrating bodies; this not only enriches the

* Corresponding author.

E-mail address: wujiang@sdu.edu.cn (J. Wu).

variety of vibrations but also facilitates the realization of compact and lightweight structure for UAs [28,29].

To date, it has been reported that the bonded-type UAs mainly work in the bending/bending (B/B), bending/longitudinal/bending (B/L), longitudinal/longitudinal (L/L), and torsional/longitudinal (T/L) vibrations [30–33]. Since the B/B actuators combine a pair of bending vibrations in identical modes but orthogonal directions, they usually do not face the obstacle of the frequency degeneration [30]. For example, Li et al. [34] designed a planar UA composed by four transducers with the B/B modes and this UA provides the resolution of 16 nm and the maximal carrying load of 35 kg. Yan et al. [35] bonded eight PZT plates onto a metal beam to form a transducer, where the maximal speed and the maximal thrust force reach 735 mm/s and 1.1 N, respectively. For most B/L actuators, the bending vibration generates the driving force while the longitudinal vibration adjusts the contacting force between the transducer and the slider. Yang et al. [36] developed a small-sized B/L actuator with the maximal speed and the output force of 487 mm/s and 2.3 N, respectively. Shi et al. [37] excited the 1st longitudinal and 2nd bending vibrations to form a V-shaped actuator, where the maximal speed and the maximal thrust force were 98 mm/s and 3.2 N, respectively. Since the electromechanical coupling effect is weaker for the bending vibration than for the longitudinal/ torsional vibrations, it would be not easy to markedly increase the thrust forces for the B/B or B/L actuators [38,39]. The L/L actuators commonly utilize the hinges that connect the longitudinal transducers as the driving feet to efficiently drive the slider. Liu et al.'s T-shaped actuator [40] used the longitudinal vibrations on the beams in the horizontal and vertical directions and it produced maximal thrust force density and maximal power density of 125 N/kg and 19.3 W/kg, respectively. Sanikhani et al. [41] applied two voltages with a phase of 180° to excite an actuator in an elliptical shape, where the maximal thrust force and the maximal speed were respectively 1.55 N and 40 mm/s. Wang et al. [42] devised a self-moving actuator by exciting dual longitudinal vibrations and achieved the maximal speed of 378 mm/s and the thrust force density of 25.5 N. However, the L/L actuators tend to be in large size because high longitudinal wave speed causes the transducers to have high resonant frequencies [30]. Since the torsional and longitudinal waves have different speeds, the combination of the T/L vibrations is commonly achieved with the clamped-type rod-shaped transducers [43], capable of generating the rotary movements rather than the translational ones. The above discussion indicates that it would be not easy to use the conventional vibrations to form the bonded-type UAs with large thrust force densities. The torsional vibration also possesses strong electromechanical effect, which facilitates the enhancement of the actuator's driving force [44]. On the other hand, the torsional wave speed is smaller than that of the longitudinal wave [30]; this implies that the usage of torsional/torsional (T/T) vibration allows the actuator to have relatively small dimensions compared to the L/L actuators. Our previous study [45] reported that, by exciting the T/T vibrations, a clamped-type actuator with the weight of 410 g provided the thrust force and the output power of respectively 96.1 N and 27.8 W. As a necessary process to fabricate the torsional clamped-type UAs, the PZT blocks are polarized in the circumferential direction; this is, however, not applicable to the bonded-type UAs because the PZT plates that bonded onto the vibrating bodies are commonly too thin to be divided for the polarizing process. Therefore, it would be meaningful to investigate the formation of the bonded-type actuator operating in the T/T vibration.

In this paper, a bonded-type transducer is designed to form a T/T actuator with high thrust force density. Here, 32 PZT plates are bonded onto the vibrating bodies to generate the torsional vibrations, and two beams transfer the torsional vibrations into a flexural traveling wave (TW). Benefiting from the operating principle, i.e., the torsional-vibration-induced TW, and the compact structure [46,47], the T/T actuator possesses the following specifications.

- (1) The block-shaped transducer has the size of $48 \times 47 \times 6 \text{ mm}^3$ and the weight of only 29 g.
- (2) In continuous operation, the T/T actuator yields the maximal sliding speed of 630 mm/s at the frequency of 24.95 kHz. Meanwhile, its maximal thrust force and maximal output power reach 4.38 N and 527.8 mW, corresponding to the thrust force density and the power density of 151.2 N/kg and 18.2 W/kg, respectively.
- (3) In stepping operation, the T/T actuator produces the minimal step displacement of 0.91 μm .

The rest of this paper is organized as follows. Section 2 describes the configuration, modeling, design, and operating principle. Section 3 shows the transducer's vibration properties. Section 4 demonstrates the actuator's movement/load characteristics. Section 5 gives the conclusions.

2. Design of T/T transducer

2.1. Configuration

As shown in Fig. 1(a), the centipede produces two TWs on both rows of legs and generates elliptical motion at the tip of each leg, which causes the entire body to move in a periodical manner [42]. It is interesting to imitate its bilateral multi-legged structure and TWs-induced movement; this can be regarded as a feature in the bionic aspect. Fig. 1(b) depicts the transducer's vibration mode, where two 2nd torsional vibrations are excited to generate bilateral standing waves (SWs) by combining the out-of-phase oscillations in d_{31} modes. In cases that the two excitation sources have both time and spatial phase differences, two flexural TWs are synthesized on bilateral beams, which drives the teeth to move in elliptical trajectories. Fig. 1(c) illustrates the basic configuration of the bonded-type T/T transducer [see Appendix A for detailed information]. The two vibrating bodies and bilateral beams made of duralumin form a block-shaped transducer in a sheet shape. To effectively excite the torsional vibration, 16 pieces of PZT plates are bonded to one side of the vibrating body with epoxy resin (E-120HP, Loctite, Dusseldorf, Germany), and other 16 PZT plates are bonded onto the other side to enhance the driving force. Each beam has nine teeth made of duralumin to enlarge the TW and realize not only compact structure but also powerful actuation. In addition, four fix parts with the size of $2 \times 2 \times 3 \text{ mm}^3$ are designed at the torsional vibration's fixed points to clamp the transducer. Fig. 1(d) demonstrates the dimensions of the transducer. The transducer has the length of l_{tr} ($= l_{ex} + 2l_{PZT}$), and the width of w_{tr} ($= 4l_{PZT} + l_0 + 2w_b$). The PZT plates have the side length l_{PZT} and thickness t_{PZT} of 10 mm and 1 mm, respectively. The undecided key dimensions will be discussed later. Moreover, 16 pieces of PZT plates are polarized along the $+z$ axis, while the adjacent PZT plates are polarized along the $-z$ axis [see Fig. 1(e)]. Besides, two sinusoidal exciting signals with the same frequency but a phase difference (φ) are required for the formation of the traveling wave. Fig. 1(f) shows the photograph of the prototype.

2.2. Dynamic model

To optimally design the T/T transducer, a dynamic model based on Mason equivalent circuit is developed to explore vibration properties and determine the key dimensions. Since the two torsional modes on two vibrating bodies have identical shapes, only half of the transducer needs to be modelled [42]. Fig. 2(a) illustrates the dimensions and the boundary conditions. Fig. 2(b) shows the model in six serially connected portions, that is, the left/right fix part, the left/right bonded part, and the left/right beam part (note that the teeth are temporarily not included in the model as we focus on the driving force in this model). The metal portions contain the acoustic impedances, while those with piezoelectric ceramics include the electromechanical coupling elements [20]. The left

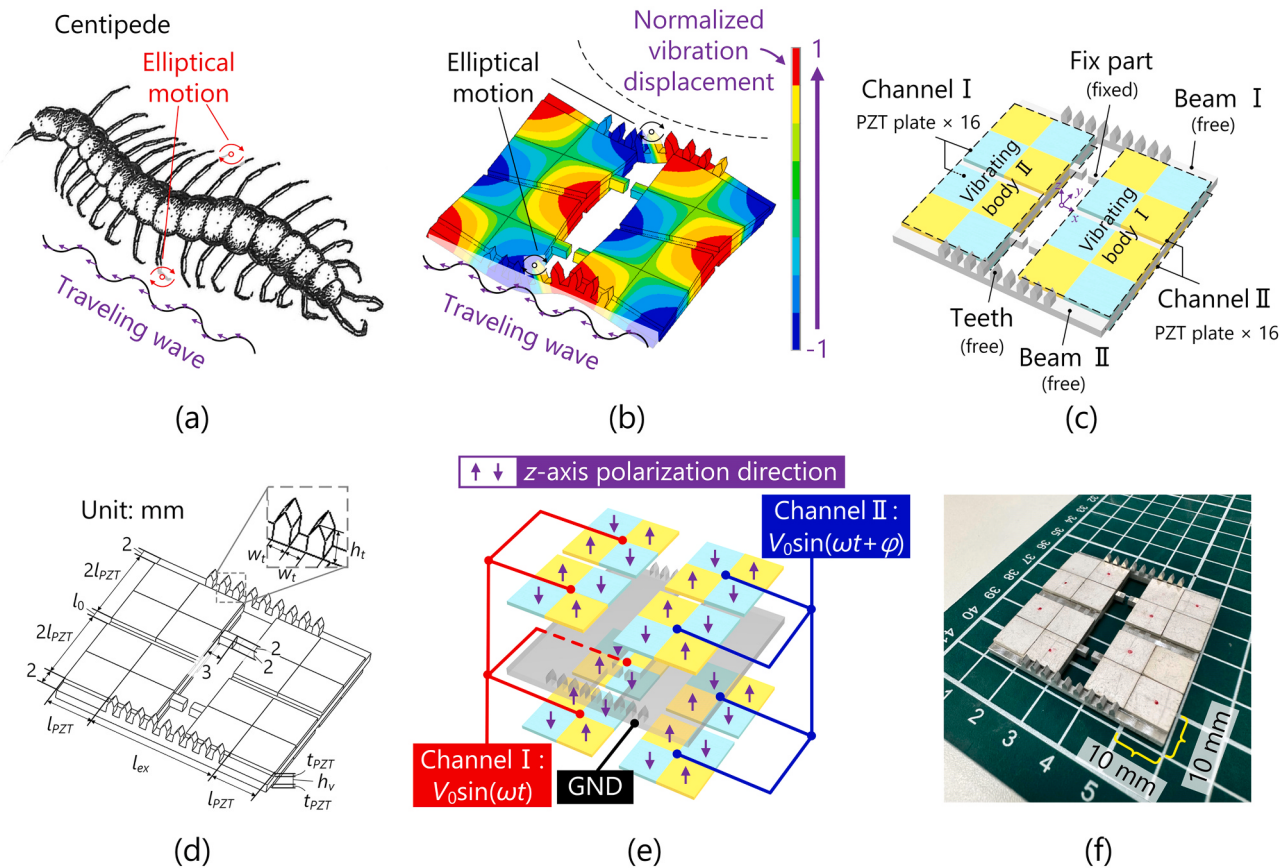


Fig. 1. Conceptual view of the ultrasonic actuator. (a) Inspiration of the centipede (adapted from the following link: <https://www.youtube.com/watch?v=Ed2wJvTRKOI>). (b) The movement pattern and dual torsional vibrations along the z-axis of the transducer. The transducer's (c) basic configuration with boundary conditions and (d) dimensions. (e) The polarization direction of the PZT plates and their connection with the electric ports. Here, ω means the angular frequency and t denotes time. (f) The photograph of the prototype.

and right sides of the model are in the open states as the transducer is clamped. In detail, the elements are described as follows.

(1) *Portion 1:* When the transducer works in the T/T mode, the elements Z_{1-1-t} and Z_{1-2-t} are expressed as [48]

$$Z_{1-1-t} = j \cdot ab \cdot \sqrt{\rho_v G_v} \cdot \tan\left(f \cdot \pi a \cdot \sqrt{\frac{\rho_v}{G_v}}\right) \quad (1)$$

and

$$Z_{1-2-t} = -\frac{j \cdot ab \cdot \sqrt{\rho_v G_v}}{\sin\left(f \cdot 2\pi a \cdot \sqrt{\frac{\rho_v}{G_v}}\right)}, \quad (2)$$

respectively, where j denotes the imaginary unit, a and b are the side length and width of the protrusion [see Fig. 1(b)], respectively, ρ_v and G_v are the vibrating body's density ($2.7 \times 10^3 \text{ kg/m}^3$) and the shear modulus (26.4 GPa), respectively, and $f [= \omega/(2\pi)]$ is the working frequency.

(2) *Portion 2:* The acoustic elements corresponding to the left bonded part can be expressed as [49]

$$Z_{2-1-t} = j \cdot l_v \cdot (h_v + 2t_{PZT}) \cdot \sqrt{\rho_2 G_2} \cdot \tan\left[f \cdot \pi \cdot \left(2l_{PZT} + \frac{l_0}{2}\right) \cdot \sqrt{\frac{\rho_2}{G_2}}\right], \quad (3)$$

and

$$Z_{2-2-t} = -\frac{j \cdot l_v \cdot (h_v + 2t_{PZT}) \cdot \sqrt{\rho_2 G_2}}{\tan\left[f \cdot \pi \cdot (4l_{PZT} + l_0) \cdot \sqrt{\frac{\rho_2}{G_2}}\right]}, \quad (4)$$

where l_{PZT} and l_0 denote the side length of the PZT plates and the interval

between groups of PZT plates [see Fig. 1(d)], respectively, and other parameters can be derived as [50]

$$\begin{cases} \rho_2 = \frac{\rho_v \cdot \left[h_v \cdot l_v \cdot \left(\frac{l_0}{2} + 2l_{PZT}\right)\right] + 8\rho_{PZT} \cdot (l_{PZT}^2 \cdot t_{PZT})}{h_v \cdot l_v \cdot \left(\frac{l_0}{2} + 2l_{PZT}\right) + l_{PZT}^2 \cdot t_{PZT}}, \\ G_2 = \frac{G_v \cdot \left[h_v \cdot l_v \cdot \left(\frac{l_0}{2} + 2l_{PZT}\right)\right] + 8c_{44} \cdot (l_{PZT}^2 \cdot t_{PZT})}{h_v \cdot l_v \cdot \left(\frac{l_0}{2} + 2l_{PZT}\right) + l_{PZT}^2 \cdot t_{PZT}}, \end{cases}, \quad (5)$$

where h_v and t_{PZT} are respectively the vibrating body's height and the PZT plate's thickness, and c_{44} (24 GPa) means the PZT plate's shear modulus orthogonal to the polarization direction. In addition, the electromechanical coupling branch includes the clamped capacitance C_{d1} and the force factor A_1 , which can be derived as [51,52]:

$$C_{d1} = \frac{2\epsilon l_{PZT}^2}{t_{PZT}}, \quad (6)$$

and

$$A_1 = \frac{16\epsilon_{31}l_{ex}}{3\pi}, \quad (7)$$

respectively, where ϵ represents the dielectric constant ($13.01 \times 10^{-9} \text{ F/m}$) and ϵ_{31} is the piezoelectric constant (-6.8 C/m^2) [53].

(3) *Portion 3:* Since it works in the bending vibration, the mechanical impedances are given as [38]

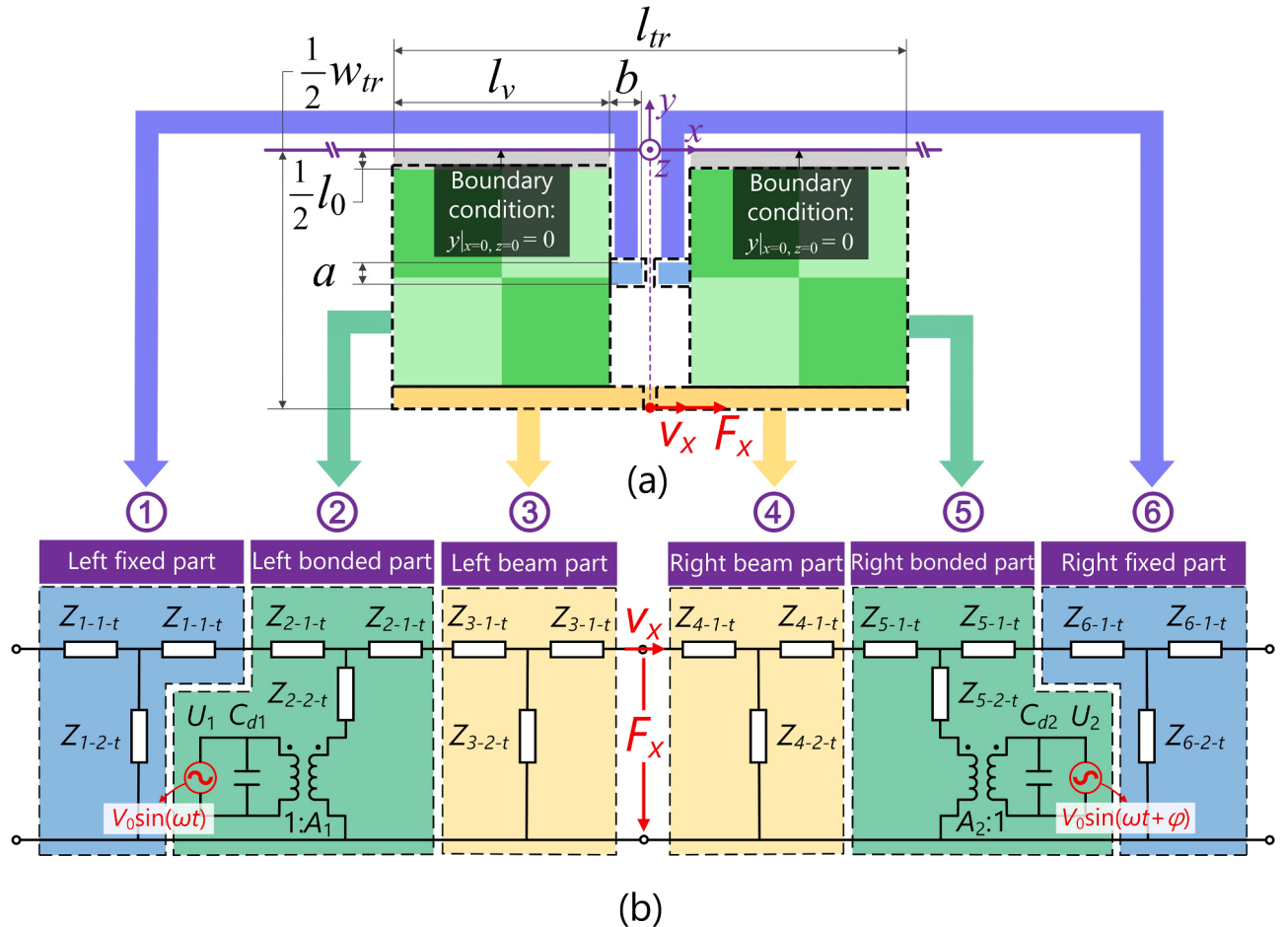


Fig. 2. Mason-equivalent-circuit-based dynamic model. (a) The key dimensions of the transducer, half of which is given for the identical configuration. (b) Model architecture. Here, v_x and F_x are the vibration velocity and the driving force at the beam's central point, respectively. After the Mason model is built in Simulink, the values of the v_x and F_x are calculated by the frequency-sweeping method [42].

$$Z_{3-1-b} = j \cdot \sqrt{2\pi f} \cdot \sqrt{\frac{E_v \rho_v^3 w_b^6 h_v^3}{12}} \cdot \tan \left(\sqrt{2\pi f} \cdot \frac{l_v}{4} \cdot \sqrt{\frac{12\rho_v}{E_v w_b^3}} \right) \quad (8)$$

and

$$Z_{3-2-b} = - \frac{j \cdot \sqrt{2\pi f} \cdot \sqrt{\frac{E_v \rho_v^3 w_b^6 h_v^3}{12}}}{\sin \left(\sqrt{2\pi f} \cdot \frac{l_v}{2} \cdot \sqrt{\frac{12\rho_v}{E_v w_b^3}} \right)}. \quad (9)$$

Here, E_v is the vibrating body's Young's modulus (71 Gpa), and l_v means the transducer's length.

(4) Portions 4, 5, and 6: For the right beam part, the right bonded part and the right fix part, the mechanical impedances and the electromechanical coupling elements of the portions 4, 5, and 6 are the same as the portions 3, 2, and 1, respectively, as a consequence of the identical dimensions [20]. Thus, the elements of the portions 4–6 are given as:

$$\begin{cases} Z_{4-1-t} = Z_{3-1-t} \\ Z_{4-2-t} = Z_{3-2-t} \\ Z_{5-1-t} = Z_{2-1-t} \\ Z_{5-2-t} = Z_{2-2-t} \\ C_{d2} = C_{d1} \\ A_2 = A_1 \\ Z_{6-1-t} = Z_{1-1-t} \\ Z_{6-2-t} = Z_{1-2-t} \end{cases}. \quad (10)$$

2.3. Design procedure

(1) *Determine each element's material.* Owing to the low density (2.7×10^3 kg/m³), duralumin (A7075) is chosen as the material of the transducer's body; and PZT plate (P4 product, Hongsheng Acoustics, China) is utilized as the ceramic element.

(2) *Decide the transducer's width and height.* The transducer's width and height deeply affect F_v , thus influencing the actuator's speed and thrust force. We employed finite element analysis (FEA) and the dynamic model to investigate F_v and F_v/m as the transducer's width (w_{tr}) and height (h_v) varied. Fig. 3(a) shows that, as w_{tr} became larger (the minimal value is set to 40 mm because sufficient space is needed for four pieces of commercially-available PZT plates), F_v exhibits monotonic enhancement at different h_v s. As depicted in Fig. 3(b), the F_v/m ratio reached its peak value at $w_{tr} = 48$ mm and $h_v = 2$ mm, which are chosen as the width and height of the transducer.

(3) *Decide the teeth's dimensions.* The width, height, and interval of the tooth are changed to make the elliptical motion close to a circular shape. Fig. 3(c) shows the kinetic model for analyzing the elliptical motion shapes. According to the geometrical relationship, the elliptical motion shape can be expressed by the B_x/B_z ratio, where B_x and B_z are the x - and z -axis vibration velocities, respectively. In specific, the B_x/B_z ratio is given as [48]

$$\frac{B_x}{B_z} = \left| \frac{v_x + \pi f w_t h_t (\sin|\alpha - \gamma| - \sin|\alpha + \gamma|)}{v_z} \right|. \quad (11)$$

Here, $\alpha = [d(v_x^2 + v_z^2)^{1/2}/dx]/\omega$, $\gamma = \arctan(w_t/h_t)$, where w_t and h_t are

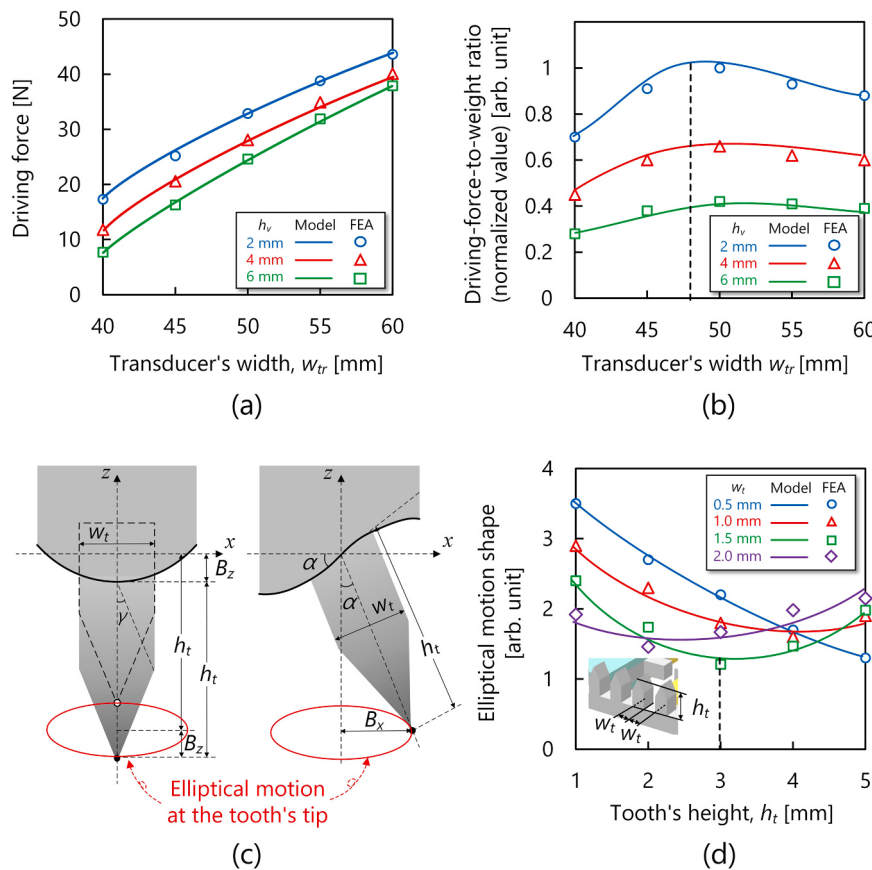


Fig. 3. Structural optimization. (a) The driving force and (b) the normalized value of the driving-force-to-weight ratio as functions of the transducer's width. (c) The kinetic model for analyzing the elliptical motion shapes. (d) The relationship between the driving teeth's elliptical motion shape and the height.

respectively the width and height of the driving tooth, and v_z is the vibration velocity along the z -axis at the beam's central point. The value of v_z can be expressed as [48]

$$v_z = \frac{j k \sigma}{2 \cdot \sqrt{\rho_v E_v \cdot d}} \cos(kx) F_x + \frac{kd\sigma}{2} \sin(kx) v_x \quad (12)$$

where j is the imaginary unit and σ is the Poisson's ratio. Fig. 4(d) illustrates the dependence of the elliptical motion shape on h_t at different w_t s. At $w_t = 1$ mm, the ratio initially decreases to 1.6 when $h_t < 4$ mm, while it increases to 1.92 when h_t varies from 4 to 5 mm. In addition, the B_x/B_z ratio reaches the minimal value of 1.21 at $h_t = 3$ mm and $w_t = 1.5$ mm, chosen as the teeth's dimensions.

(4) Decide the length of the transducer. When two channels of driving voltage with a phase φ are applied to the transducer, the TW propagation along the x -axis on the beam is expressed as [48]

$$\begin{aligned} w(x, t) &= A \cos(kx) \cos(\omega t) + A \cos[k(x + l_{ex})] \cos(\omega t + \varphi) \\ &= A \cos\left[\frac{1}{2}(kl_{ex} + \varphi)\right] \cos\left[\omega t + kx + \frac{1}{2}(kl_{ex} + \varphi)\right] \\ &\quad + A \cos\left[\frac{1}{2}(kl_{ex} - \varphi)\right] \cos\left[\omega t + kx + \frac{1}{2}(kl_{ex} - \varphi)\right], \end{aligned} \quad (13)$$

where A represents the vibration amplitude, l_{ex} stands for the distance between two excitation sources on each beam, k stands for the wave-number, and ω represents the angular frequency ($\omega = 2\pi f$). To effectively excite the flexural TW on two beams, it is needed that [45]

$$\frac{1}{2}(kl_{ex} \pm \varphi) = \frac{1}{2}\left(\frac{2\pi}{\lambda_B}l_{ex} \pm \varphi\right)l_{ex} = \frac{2n+1}{4}\cdot\pi, \quad (14)$$

where n is an integer and $\lambda_B (= 2\pi/k)$ is the wavelength corresponding to

the bending vibration. At $n = 0$, there is no sufficient space for the two PZT plates (20 mm). Considering the requirement of weight reduction, we set that

$$l_{ex} = \frac{3}{4}\lambda_B = 1.01 \cdot \left(\frac{h_v}{f}\right)^{\frac{1}{2}} \cdot \left(\frac{E_v}{\rho_v}\right)^{\frac{1}{4}}, \quad (15)$$

where h_v means the vibrating body's height. In this case, l_{ex} is set as 27 mm. When the lengths of two PZT plates are included, the transducer's length is finally determined as 47 mm.

2.4. Operating principle

Fig. 4 illustrates the T/T transducer's operating principle. When two torsional vibrations with a certain phase are excited at the vibrating bodies, the synthesized wave can be expressed as:

$$\begin{aligned} x(\omega, t) &= x_1(\omega, t) + x_2(\omega, t) \\ &= \cos(\omega t) \cos(kx) + \cos(\omega t + \varphi) \cos(kx + \theta) \\ &= \cos(\omega t) \cos(kx) + \cos\left(\omega t + \frac{\pi}{2}\right) \cos\left(kx + \frac{3\pi}{2}\right) \\ &= \cos(\omega t + kx) \end{aligned} \quad (16)$$

where θ denotes the phase difference in space. Accordingly, their superposition leads to a TW in the $+x$ direction on the bilateral beams. The motion at the teeth's tip exhibits a counterclockwise elliptical trajectory, which frictionally drives the slider to move in the $-x$ direction. In addition, owing to the torsional deformation being symmetric about the xz -plane, the propagation of the TWs on bilateral beams are in the same direction, thus ensuing the transducer's linear motion. Reverse movement can be easily achieved by simply changing the phase difference

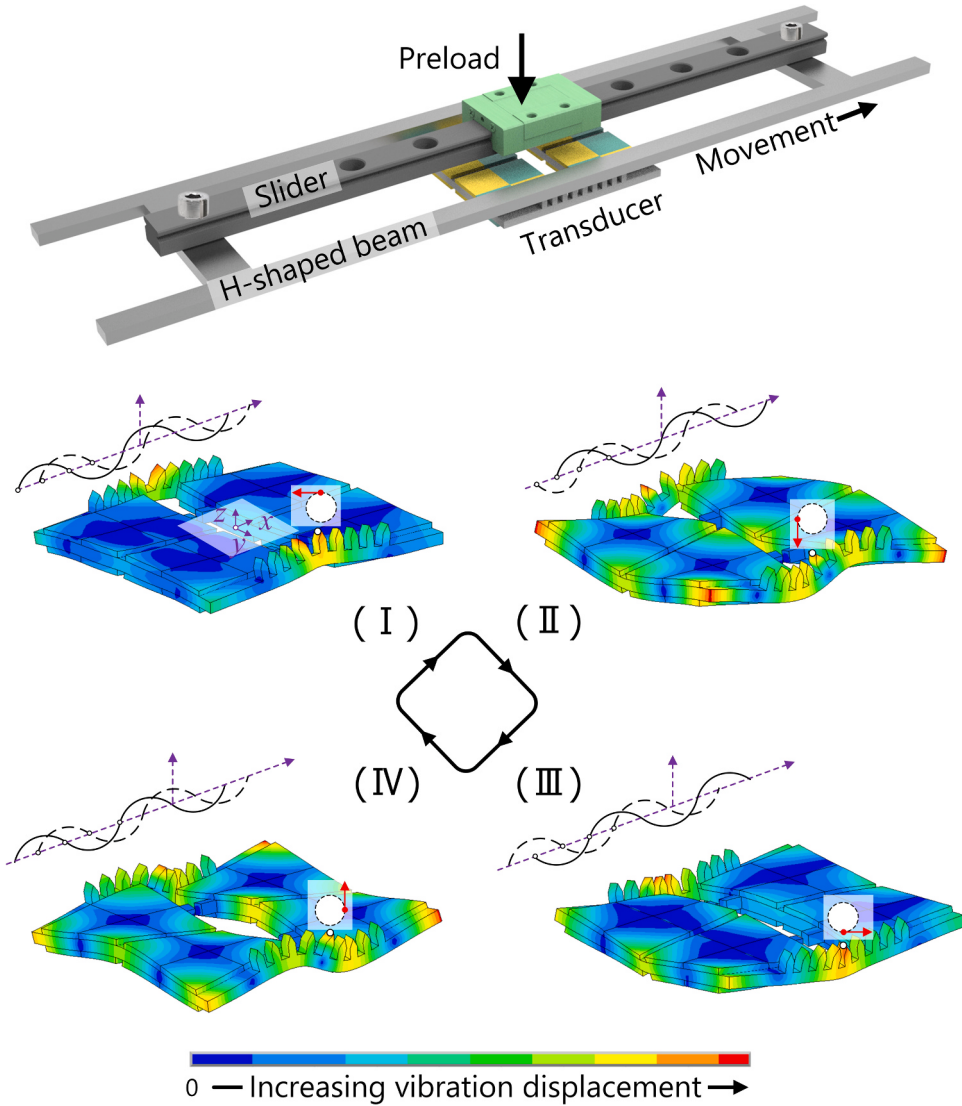


Fig. 4. Operating principle of the transducer.

from $+90^\circ$ to -90° .

3. Vibration properties

3.1. Vibration velocity distributions

Initially, the vibration properties were investigated to test whether the vibrations and the TWs were excited as predicted. As shown in Fig. 5(a), the vibration properties were measured with a scanning laser Doppler vibrometer (LDV; PSV-500, Polytec, Waldbronn, Germany). The voltages were applied to the PZT plates with the bipolar power amplifiers. By scanning the actuator's surface, the 2nd torsional vibrations were clearly observed [see Fig. 5(b)], and the TWs on bilateral beams indicate the effectiveness of the excitation.

Subsequently, the vibration velocity distributions on two beams were evaluated to further verify the successful excitation of TWs, where the working frequency (f), the driving voltage (V_0), and the phase difference between the two channels (φ) were set to 24.95 kHz, 250 V, and 80° , respectively (note that, the voltage and the vibration velocity are indicated as the zero-to-peak values in this article). Fig. 5(c) illustrates that the average vibration velocity is 743 mm/s on beam I, and the phase difference relative to $x = 0$ (ψ) gradually decrease from 138° to -136° . Fig. 5(d) shows the average vibration velocity of 749 mm/s on

beam II, and ψ decreases from 132° to -133° . These results demonstrate the successful excitation of TWs on the bilateral beams [6].

3.2. Standing wave ratio

Followingly, the variation in the SW ratios against the phase was investigated to evaluate the synthesis quality of the TWs. Here, the SW ratio is defined as the v_{max}/v_{min} ratio, where v_{max} and v_{min} represent the maximal and minimal vibration velocities, respectively [45]. Considering that two SWs have a spatial phase difference of $3\pi/2$ and a phase difference of φ in the time domain, the waves propagation on the beams can be expressed as

$$\begin{aligned} w(t, x) &= A \cos(\omega t) \cos(kx) + A \cos(\omega t + \varphi) \cos\left(kx + \frac{3}{2}\pi\right) \\ &= A \cos\left(\omega t + \frac{2\pi}{\lambda_B} \cdot x\right) + A \sin\left(\frac{2\pi}{\lambda_B} \cdot x\right) [\sin(\omega t) - \cos(\omega t + \varphi)], \end{aligned} \quad (17)$$

where A denotes vibration amplitude. At $\omega t = 0$, magnitudes of the TW and SW components are equal to respectively $|A|$ and $|A \cos(\varphi)|$. Here, the SW ratio is referred to as [54]

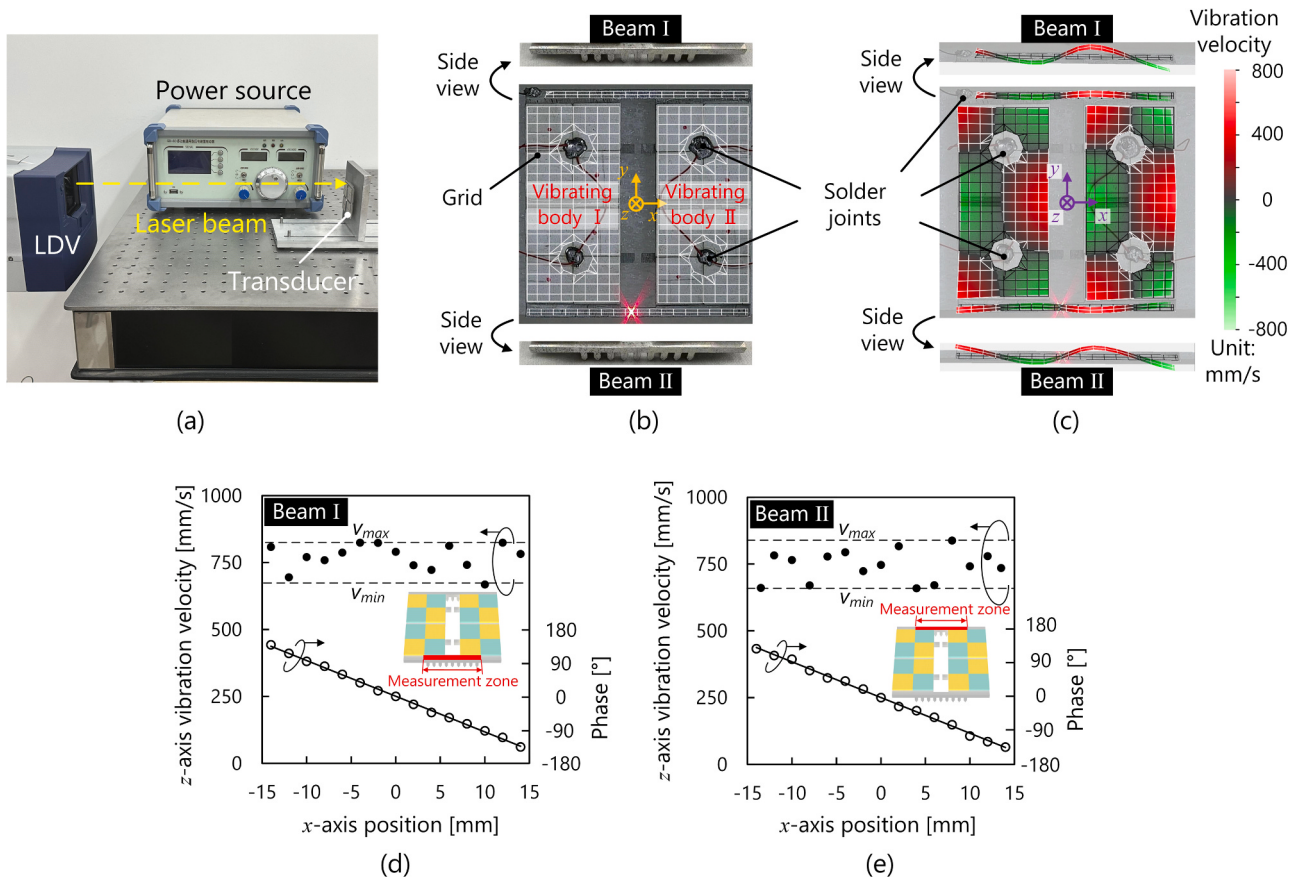


Fig. 5. Vibration properties. (a) The testbed for measuring the vibration properties. (b) The observation direction of the transducer, where the grids are marked. (c) The scanning results, which indicate the effective excitation of the 2nd torsional vibrations and traveling waves. The vibration velocity distributions on (d) the beam I and (e) beam II.

$$SW \text{ ratio} = \frac{1 + |\cos(\varphi)|}{1 - |\cos(\varphi)|}. \quad (18)$$

Fig. 6(a) and (b) illustrate the relationship between the SW ratios and the phase difference in the time domain (φ) on beam I and beam II, respectively. It is observable that the theoretical and experimental results show the same tendencies approximately. In addition, when the phase differences are -100° or 80° , the SW ratios exhibit minimal values

of 1.24 and 1.27 on beam I and beam II, respectively.

3.3. Vibration velocities versus driving voltage

Afterwards, the vibration velocities on two beams were explored as the driving voltages varied. During the test, we set $f = 24.95$ kHz and $\varphi = 80^\circ$. As shown in Fig. 7(a), the vibration velocity on beam I exhibits a monotonic enhancement as the driving voltage increases, and reaches its

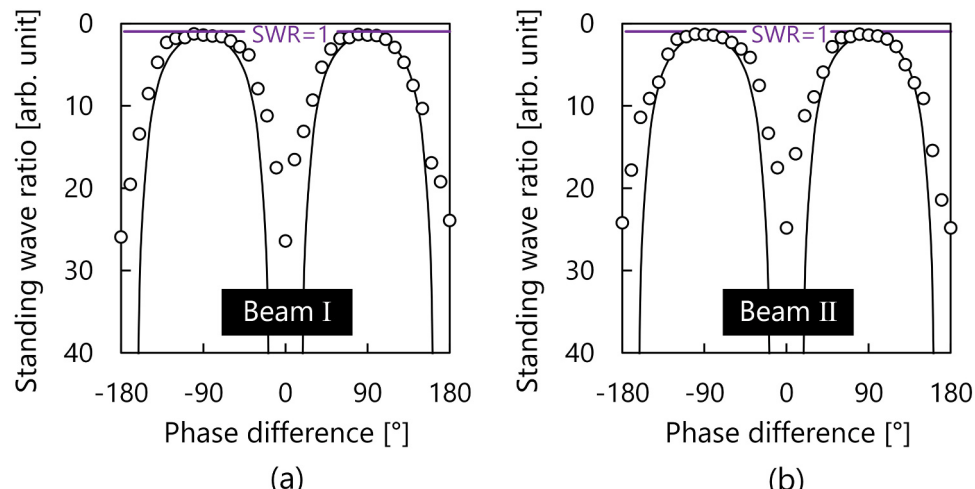


Fig. 6. Standing wave ratio as functions of the phase difference in the time domain on (a) beam I and (b) beam II. The experimental results are given as the dots and the theoretical results are indicated as the black curves.

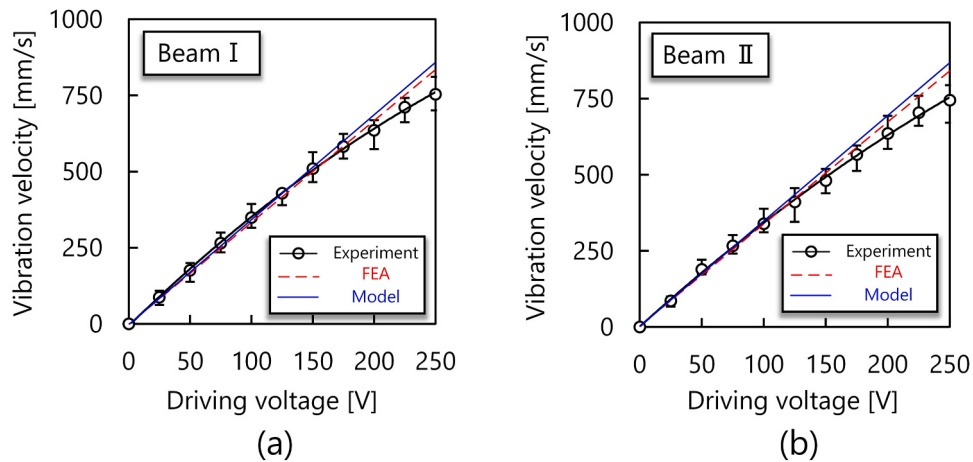


Fig. 7. Vibration velocities on (a) beam I and (b) beam II as functions of the driving voltages.

maximal value of 753.7 mm/s at $V_0 = 250$ V. Fig. 7(b) illustrates the similar tendency on beam II except that the maximal vibration velocity is 744.6 mm/s. The experiment results are consistent with the theoretical results obtained by FEA and the model.

3.4. Verification of elliptical motion

Finally, the middle feet's vibration displacements in orthogonal directions were measured at $f = 24.95$ kHz, $V_0 = 250$ V, and $\varphi = 80^\circ$. Fig. 8(a) illustrates that, at the middle foot on beam I, the vibration displacements on the x - and z -axis are 5.4 and 5.3 μm , respectively. The orthogonal displacements supervised to form an ellipse in the xz -plane

[see Fig. 8(b)], which is consistent with the results obtained by the model and FEA. Fig. 8(c) and (d) show the vibration displacements and the synthesized elliptical trajectory of the middle driving foot on beam II, respectively. Accordingly, the similar circular shapes demonstrate the effective design and efficient actuation.

4. Actuator's performance

4.1. Experimental setup

Fig. 9(a) shows the testbed for estimating the actuator's performance, which was installed onto a horizontal platform. The thrust force

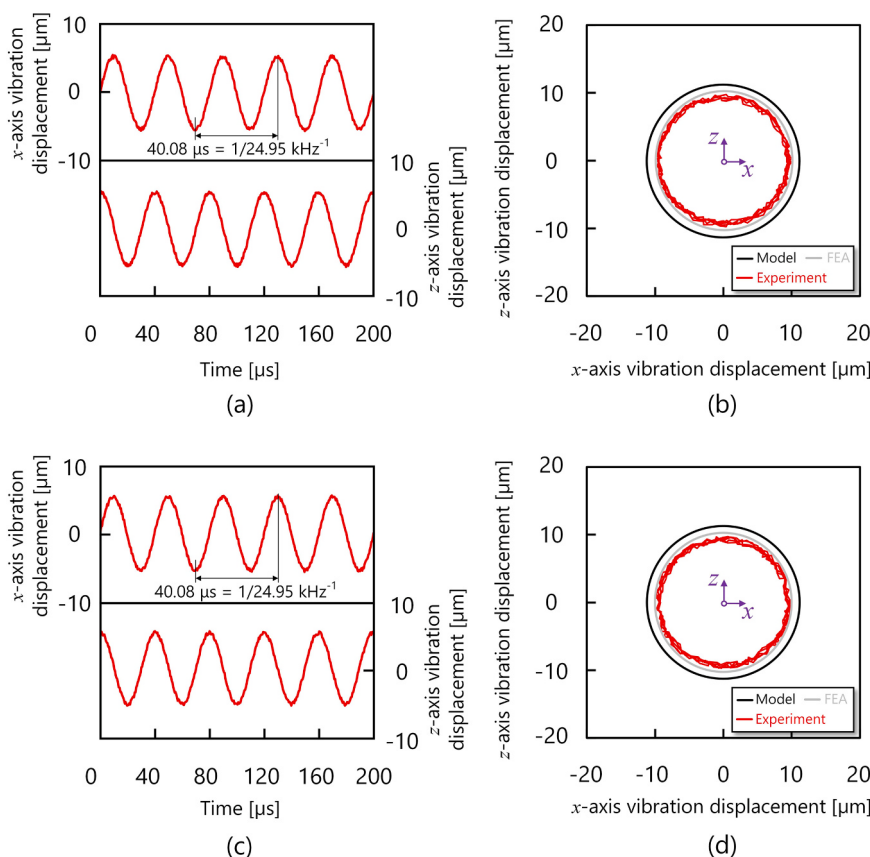


Fig. 8. Elliptical motion verification. (a) Vibration displacements in the time domain and (b) the formation of the elliptical trajectory at the middle driving foot on the beam I. (c) Vibration displacements in the time domain and (d) formation of the elliptical trajectory at the middle driving foot on the beam II.

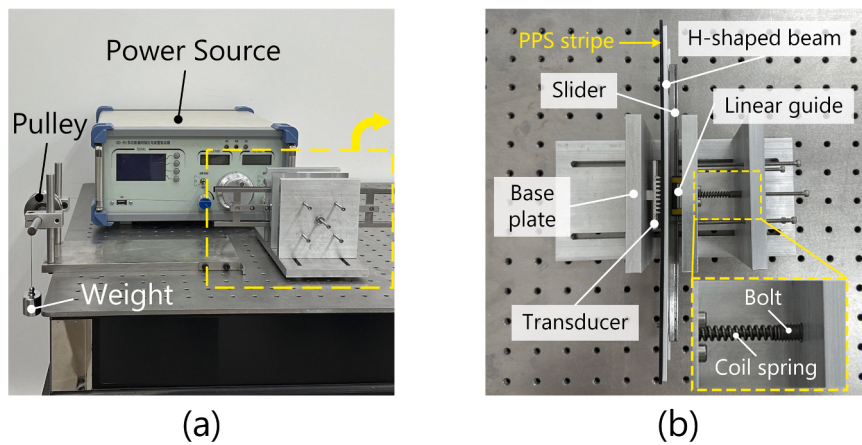


Fig. 9. Experiment setup for evaluating the actuator's performance. (a) Lateral view and (b) vertical view.

was estimated by pulling up weights, the sliding speed was measured with a laser displacement sensor (WT53R, Wit-motion Technology Corporation, Guangzhou, China), and the input power was measured with a power meter (3332, Hioki, Nagano, Japan). **Fig. 9(b)** illustrates the configuration of the actuator. One side of the transducer was fixed to a vertical base plate to eliminate the influence of gravity on the load characteristics. The other side (driving teeth) contacted a H-shaped beam whose surface was bonded with PPS strips (Young's modulus: 3.45 GPa, Poisson's ratio: 0.36, density: $1.35 \times 10^3 \text{ kg/m}^3$) [50,51], and the H-shaped beam was bolted to the slider. Besides, the preload to the transducer was applied by compressing a coil spring and adjusting by rotating the bolt, where the force was estimated from the spring-stiffness coefficient and the spring's deformation.

4.2. Continuous movement characteristics

Initially, the actuator's sliding speeds as functions of the electrical parameters were investigated. **Fig. 10(a)** illustrates the sliding speed's dependence on the working frequency. At $f = 24.95 \text{ Hz}$, the actuator reached to the maximal sliding speed of 630.7 mm/s at $V_0 = 250 \text{ V}$ and 216.9 mm/s at $V_0 = 100 \text{ V}$. Observably, as the frequency deviated from the resonant frequency, the speed exhibited a sharp reduction. **Fig. 10(b)** shows the relationship between the sliding speed and the phase difference. The speed initially increased and reached the peak values in the negative direction at about -100° ; and they became lower as the phase increased from -100° to 0° , and got the maximal value in the positive direction at 80° . The curve shows a similar tendency when the voltage is 100 V . **Fig. 10(c)** shows how the driving voltage affects the sliding speed. The sliding speeds had nearly linear relationship with $V_0 > 37 \text{ V}$; this facilitates the easy adjustment of the sliding speed.

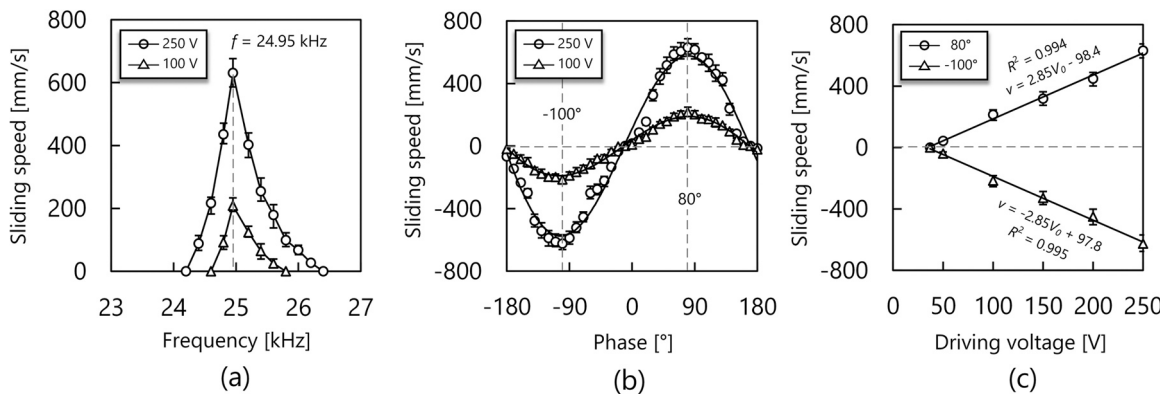


Fig. 10. Movement characteristics during continuous operation. The sliding speed as functions of (a) frequency, (b) phase, and (c) voltage.

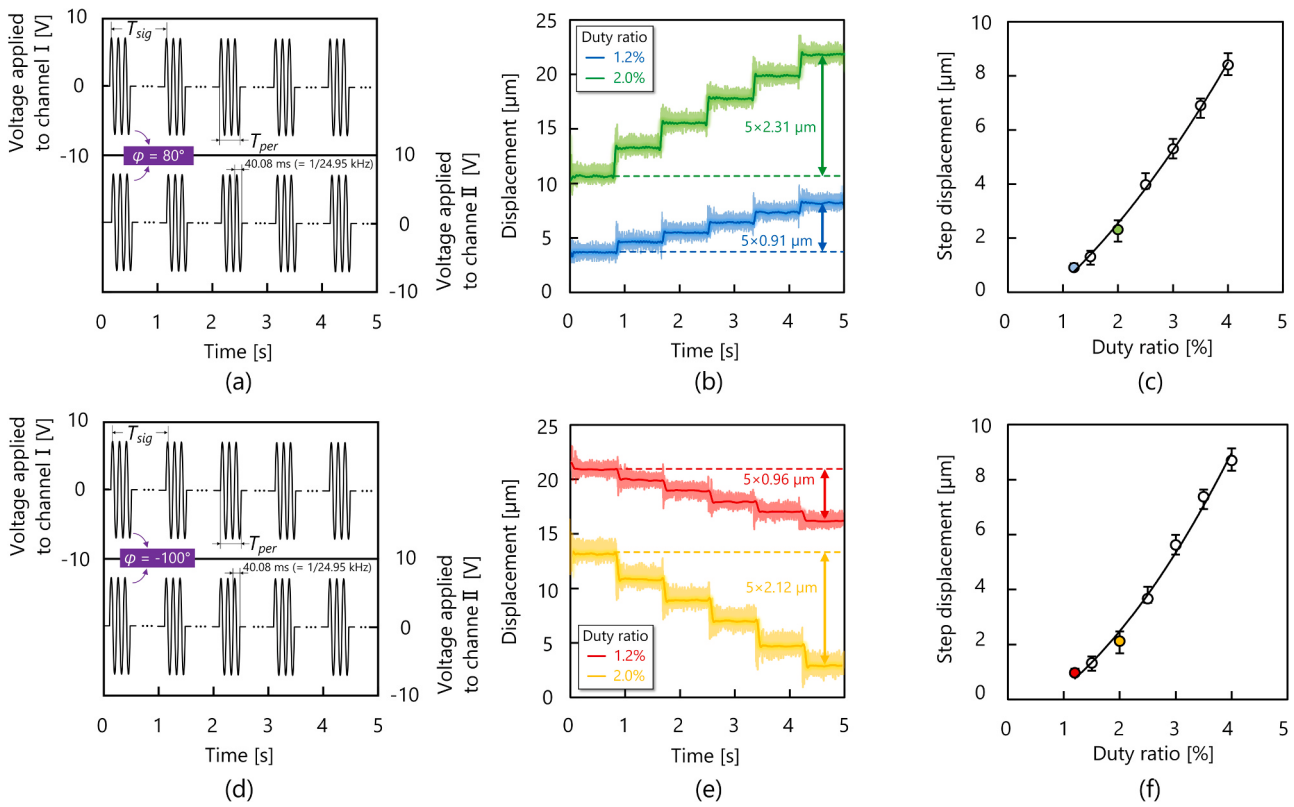


Fig. 11. Movement characteristics during the stepping operation. (a) Exciting signals, (b) the stepwise displacement in the time domain, and (c) the step displacement as functions of the duty ratio when the actuator moves in the $+x$ direction. (d) Exciting signals, (e) the stepwise displacement in the time domain, and (f) the step displacement as functions of the duty ratio when the actuator moves in the $-x$ direction.

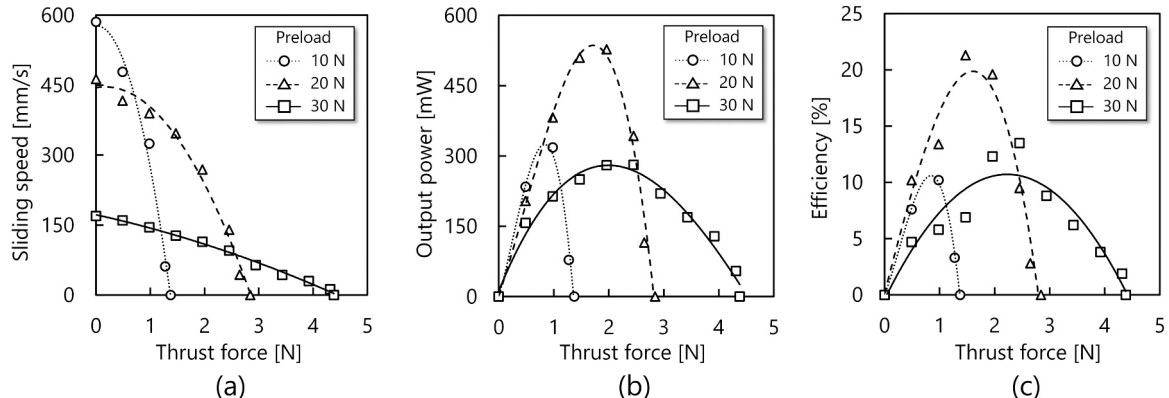


Fig. 12. Load characteristics of the actuator at $f = 24.95 \text{ kHz}$, $V_0 = 250 \text{ V}$, and $\varphi = 80^\circ$. (a) Sliding speed, (b) output power, and (c) efficiency as functions of the thrust force.

thrust force. The actuator produced the maximal output power of 527.4 mW at the moderate preload and thrust force of 20 N and 1.96 N, respectively. Fig. 12(c) depicts that, at 20 N preload, the actuator's maximal efficiency was 21.3 % when thrust force was 1.47 N.

Afterwards, Fig. 13(a), (b), (c), and (d) respectively depict the variations in no-load sliding speed, maximal torque, maximal output power, and maximal efficiency, versus the driving voltage at different preloads. Observably, the no-load sliding speed linearly increased as the driving voltage became higher owing to the enhancement in the torsional vibration velocity. At $V_0 = 250 \text{ V}$, the actuator's sliding speed reached 585.7, 463.3, and 169.3 mm/s, respectively. The thrust force gradually increased as the voltage became higher, but leveled off at a certain voltage, probably because the frictional force had reached its maximal value. The maximal output power became higher as the voltage

increased. The maximal output power and the maximum efficiency existed when the preload was set to 20 N. Accordingly, the thrust force density and the power density reach 151.2 N/kg and 18.2 W/kg, respectively.

4.5. Performance comparison

Finally, the proposed actuator was compared with other typical linear actuators/motors. The results listed in Table 1 indicate the following conclusions.

- (1) The sliding speed, maximal output power, and maximal efficiency of our actuator are 4.4, 3.5, and 2.3 times larger than Shi et al.'s [37] ultrasonic motor, respectively; this indicates the

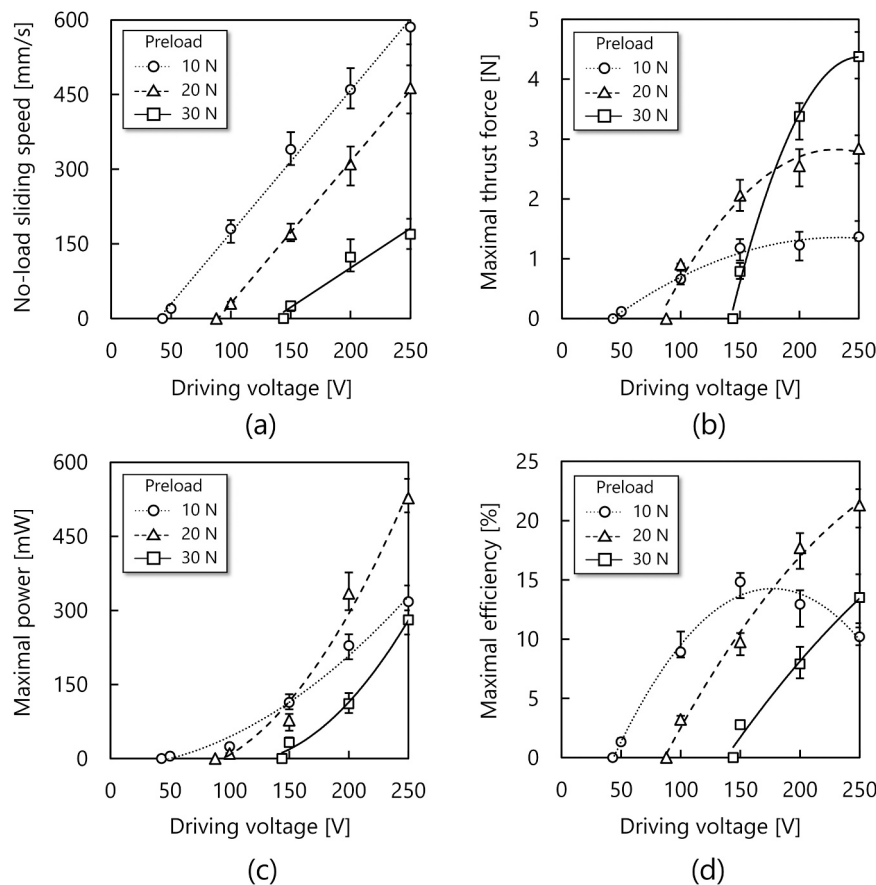


Fig. 13. Load characteristics of the actuator with varying voltage. (a) No-load sliding speed, (b) maximal thrust force, (c) output power, and (d) efficiency versus the driving voltage under varying preloads.

Table 1
Performance comparison between the developed actuator and typical ones.

	This study	[37]	[55]	[56]	[57]	[42]
Vibration modes	T/T	L/B	L/B	B/B	B/B	L/L
Dimension [mm ³]	48×47×6	40×10×5	45.7×Φ30	74×10×10	49×12.5×12.5	87.5×9×9
Transducer's weight [g]	29.0	18.0	19.3	20.4	17.7	15.7
Working frequency [kHz]	24.95	53.50	30.20	34.72	62.40	105.44
Maximal thrust force [N]	4.38	2.80	0.39	3.50	0.76	0.40
No-load sliding speed [mm/s]	630.7	142.0	1103.0	117.2	208.0	378.0
Maximal output power [mW]	527.4	149.5	62.0	136.9	NA	NA
Maximal efficiency	21.3 %	9.1 %	18.8 %	NA	NA	NA
Thrust force density [N/kg]	151.2	155.3	20.3	171.6	42.9	25.5
Power density [W/kg]	18.2	8.3	3.2	6.7	NA	NA

effectiveness of our actuator's driving principle. In addition, Shi et al.'s SW motor can only move in one direction, limiting the motor's practical application.

- (2) Although the sliding speed of our actuator is inferior to Ding et al.'s [55] linear motor, the actuator's thrust force density and power density are 7.4 times and 5.7 times greater than that of Ding et al.'s motor, respectively; this is primarily caused by the relatively high rigidity of the duralumin-based transducer. In addition, our actuator takes two same vibration modes, meaning that the frequency degeneration is not needed, which enhances the electromechanical conversion efficiency and reduces the heating problem [30].
- (3) Due to the low electromechanical coupling factor of the bending/bending motor/actuator, the power density of the three-feet ultrasonic motor proposed by Li et al. [56] is 0.37 times that of our actuator. Besides, our actuator achieves a higher sliding speed of

630.7 mm/s, which is 5.4 times greater than that of Li et al.'s motor. Same issue is observed in Liu et al.'s [57] actuator, which yields approximately one-third the sliding speed and thrust force density compared to our actuator; this indicates the output advantages of the T/T mode.

- (4) Inspired by the millipede's movement, Wang et al. [42] develops a longitudinal-vibration-induced TW actuator, where the teeth swing as the longitudinal TW oscillates; this results in an inferior driving force than the transverse traveling wave in our actuator, leading to both lower speed and thrust force.

In summary, the T/T actuator accomplishes relatively high thrust force density and high power density compared to most of the listed actuators; this validates the effectiveness of our proposal.

5. Conclusion

This article presented the proposal, design, and performance evaluation of the T/T actuator. Through numerical analysis and experimental investigation, we have drawn the following conclusions.

- (1) Inspired by the centipede, a bonded-type ultrasonic actuator was developed by exciting the T/T vibrations and its feasibility was verified by evaluating the moving/loading performance.
- (2) A Mason-equivalent-circuit-based dynamic model was employed to determine the key dimensions of the T/T transducer.
- (3) When two channels of voltages with a certain phase were applied, two torsional vibrations were excited to generate a pair of TWs on the bilateral beams, which frictionally drive the slider.
- (4) At the frequency and voltage of respectively 24.95 kHz and 250 V, the actuator produces the sliding speed, the maximal thrust force, the maximal output power, and the maximal efficiency of 630 mm/s, 4.38 N, 527.8 mW, and 21.3 %, respectively. Moreover, it yields the thrust force density and the power density of 151.2 N/kg and 18.2 W/kg, respectively.

These conclusions not only validate the effectiveness of our proposal but also provide a new approach to design the T/T transducer. In the future, we will concentrate on the optimization of the friction conditions between the transducer and the slider as it facilitates the improvement in the efficiency and the moving stability. Besides, it would be worthwhile to apply other bionic-inspired configuration to design/fabricate the actuators.

CRediT authorship contribution statement

Xiaojia Zhu: Investigation, Data curation. **Xiaoming Yue:** Writing –

Appendix A. Structure, fix method, and admittance characteristics of the transducer

First, to demonstrate the structures as well as the dimensions of the transducer (including the teeth), a three-view drawing of the transducer is given in Fig. A1. Clearly, the transducer is in plate shape while a series of teeth are created on two beams.

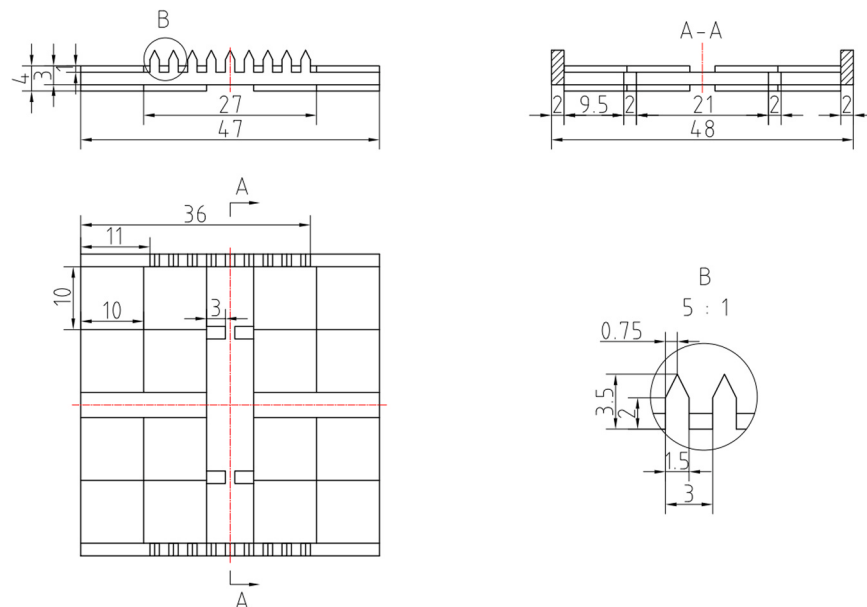


Fig. A1. Three-view drawing of the transducer.

review & editing, Investigation, Formal analysis. **Leilei Lv:** Visualization, Software. **Yili Wang:** Software, Investigation. **Xuhui Jing:** Visualization, Data curation. **Lipeng Wang:** Software, Methodology, Data curation. **Zhaochun Ding:** Software, Data curation. **Jiang Wu:** Writing – review & editing, Supervision, Project administration, Funding acquisition, Conceptualization. **Xiaohang Lai:** Validation, Data curation. **Chengqi Pan:** Resources, Methodology, Investigation, Data curation. **Longhui Ding:** Formal analysis, Data curation. **Jinshuo Liu:** Writing – original draft, Validation, Investigation, Formal analysis, Data curation, Conceptualization.

Declaration of Competing Interest

The authors declare that they have no known competing financial interests or personal relationships that could have appeared to influence the work reported in this paper.

Data availability

Data will be made available on request.

Acknowledgement

This work was partially supported by National Natural Foundation of China (NSFC) (No. 52105029), Science Center Program of NSFC (No. 62188101), Natural Science Foundation of Shandong Province (ZR2021QE020), Foundation of Taishan Scholar Project (tsqn202306052), Research Project jointed by Shandong University and Geortek Inc. (HTGIT20230011), Shandong Provincial Major Scientific and Technological Innovation Project (2021CSGC011207).

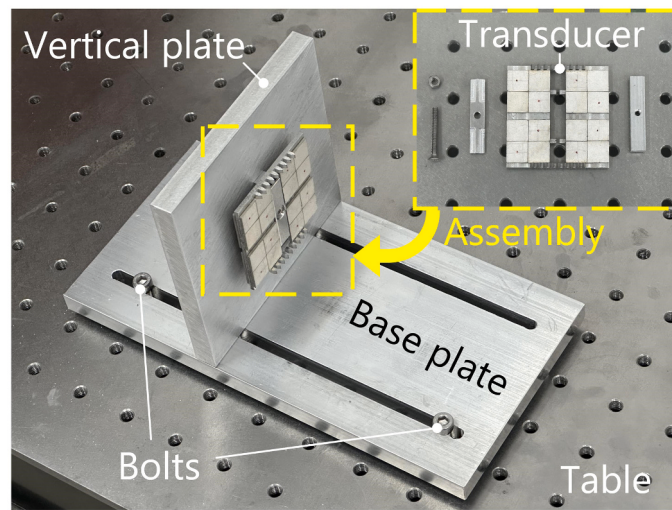


Fig. A2. Photo of the fix method of the transducer.

Then, the fix method of the transducer is discussed to achieve its effective operation. As shown in Fig. A2, the base plate is arranged onto the table with bolts, a vertical plate is fixed to the base plate, and the transducer is mounted onto the vertical plate.

Finally, to demonstrate that the torsional mode dominantly exists at the working frequency, we explore the admittance characteristics of the transducer. As shown in Fig. A3(a), the admittance characteristic was measured with an impedance analyzer (ZX70AX, Zhixin Precision Electronics, Changzhou, China). As plotted in Fig. A3(b), the torsional vibration has the resonant frequency (f_r) and anti-resonant frequency (f_a) of 24.95 and 25.45 kHz, respectively, and its electromechanical coupling factor k is estimated as 19.7 % according to the following equation [1], [3]:

$$k = \sqrt{1 - \left(\frac{f_r}{f_a}\right)^2}. \quad (\text{C1})$$

Though the bending and longitudinal vibrations can be found at respectively $f_r = 23.89$ and 27.08 kHz, their k s are 9.2 % and 15.5 %, relatively small compared to the value of the torsional vibration; this implies the torsional vibration is, as predicted, dominantly excited with the transducer.

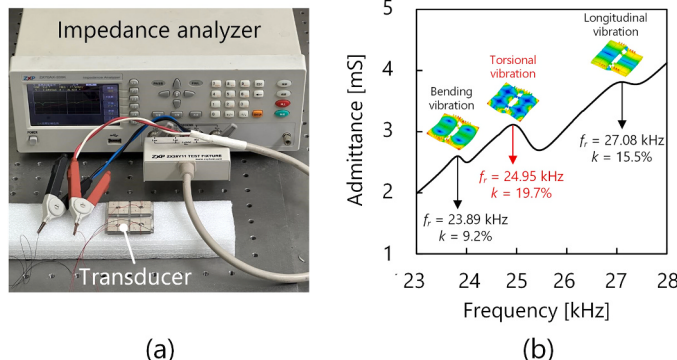


Fig. A3. Admittance characteristics of the transducer. (a) The testbed and (b) the measurement results.

References

- [1] J. Wu, Y. Mizuno, K. Nakamura, Polymer-based ultrasonic motors utilizing high-order vibration modes, *IEEE/ASME Trans. Mechatron.* 23 (2) (2018) 788–799.
- [2] R. Wang, L. Wang, B. Jia, J. Jin, D. Wu, Semi-analytical modeling and experimental evaluation on a novel standing wave rotary piezoelectric actuator driven by single-phase signal, *Mech. Syst. Signal Process.* 163 (Jan. 2022) art. no. 108177.
- [3] W. Wei, Z. Ding, J. Wu, L. Wang, C. Yang, X. Rong, R. Song, Y. Li, A miniature piezoelectric actuator with fast movement and nanometer resolution, *Int. J. Mech. Sci.* 273 (2024) art.no. 109249.
- [4] W. Sun, Z. Xu, K. Wang, X. Li, J. Tang, Z. Yang, H. Huang, An impact inertial piezoelectric actuator designed by means of the asymmetric friction, *IEEE Trans. Ind. Electron.* 70 (1) (2023) 699–708.
- [5] J. Zhao, G. Mu, H. Dong, T. Sun, K.T.V. Grattan, Study of the velocity and direction of piezoelectric robot driven by traveling waves, *IEEE Trans. Ind. Electron.* 70 (9) (2023) 9260–9269.
- [6] S. Guo, L. Wang, J. Jin, Y. Yang, A general structural design method, dynamics modeling, and application study for built-in sandwich annular traveling wave piezoelectric transducers, *Mech. Syst. Signal Process.* 199 (2023) art. no. 110476.
- [7] J. He, Y. Chen, B. Cao, X. Li, T. Yang, Z. Hu, L. Ran, W. Zhou, Traveling wave distortion of MEMS ultrasonic motor induced by anisotropic elasticity, *Mech. Syst. Signal Process.* 189 (2023) art. no. 110083.
- [8] K. Li, J. Sun, S. He, X. Zhou, H. Li, Y. Liu, On-demand preparation of calcium alginate microspheres via piezoelectric microfluidics, *Sens. Actuators A* 347 (2022) art. no. 113925.
- [9] Z. Wen, D. Wu, and K. Nakamura, “A miniature traveling wave ultrasonic linear motor utilizing bimorph transducers,” *IEEE Trans. Ultrason. Ferroelectr. Freq. Control*, in press. doi: 10.1109/TUFC.2024.3395525.
- [10] Y. Wang, J. Deng, S. Zhang, H. Li, W. Chen, Y. Liu, Design of a linear-rotary ultrasonic motor for optical focusing inspired by the bionic motion principles of the earthworms, *Int. J. Smart Nano Mater.* 13 (2) (2022) 346–365.
- [11] J. Deng, J. Li, K. Yan, Y. Liu, Development of a miniature piezoelectric robot with high stability and strong load capacity based on hexapod of radial layout, *IEEE/ASME Trans. Mechatron.* 29 (1) (2024) 754–766.
- [12] X. Ma, Y. Liu, J. Liu, J. Deng, Crabbot: a pole-climbing robot driven by piezoelectric stack, *IEEE Trans. Robot.* 38 (2) (2022) 765–778.
- [13] S. Mohith, A.R. Upadhyaya, K.P. Navin, S.M. Kulkarni, M. Rao, Recent trends in piezoelectric actuators for precision motion and their applications: a review, *Smart Mater. Struct.* 30 (1) (2020) art. no. 013002.

- [14] Y. Hu, J. Ma, Y. Zhang, J. Li, Y. Hu, J. Wen, Performance comparison of two motion modes of a piezoelectric inertial linear motor and its potential application in cell manipulation, *Mech. Syst. Signal Process.* 157 (2021) art. no. 107743.
- [15] Z. Li, R. Zhu, X. Yi, S. Dong, “A high-power-density piezoelectric actuator operating in bicycling movement mechanism, *IEEE Trans. Ind. Electron.* 70 (6) (2023) 6090–6098.
- [16] T. Cao, X. Li, Z. Wen, B. Wang, W. Liu, D. Yu, D. Wu, A CFRP/PZT laminated piezoelectric motor with high force density, *Smart Mater. Struct.* 30 (7) (2021) art. no. 075005.
- [17] H. Jin, X. Gao, K. Ren, J. Liu, L. Qiao, M. Liu, W. Chen, Y. He, S. Dong, Z. Xu, F. Li, Review on piezoelectric actuators based on high-performance piezoelectric materials, *IEEE Trans. Ultrason. Ferroelectr. Freq. Control* 69 (11) (2022) 3057–3069.
- [18] L. Wang, Y. Guan, Y. Liu, J. Deng, J. Liu, A compact cantilever-type ultrasonic motor with nanometer resolution: design and performance evaluation, *IEEE Trans. Ind. Electron.* 68 (1) (2021) 734–743.
- [19] D. Xu, W. Yang, X. Zhang, S. Yu, T. Liang, A U-shaped and alternately driven ultrasonic motor using three bending coupled modes, *Smart Mater. Struct.* 32 (3) (2023) art. no. 035017.
- [20] W. Wei, J. Wu, Z. Ding, J. Liu, Z. Cao, Y. Liu, K. Wang, C. Xing, A linear ultrasonic motor driven by torsional/bending vibrations, *Sens. Actuators A* 357 (2023) art. no. 114404.
- [21] K. Yokoyama, H. Tamura, K. Masuda, T. Takano, Single-phase drive ultrasonic linear motor using a linked twin square plate vibrator, *Jpn. J. Appl. Phys.* 52 (7S) (2013) art. no. 07HE03.
- [22] Y. Liu, J. Yan, L. Wang, W. Chen, “A two-DOF ultrasonic motor using a longitudinal-bending hybrid sandwich transducer,” *IEEE Trans. Ind. Electron.* 66 (4) (2019) 3041–3050.
- [23] Q. Zhang, S. Piao, H. Chen, J. Wu, K. Nakamura, “A linear piezoelectric actuator using ‘A-shaped’ structure,” *IEEE Trans. Ultrason. Ferroelectr. Freq. Control* 69 (4) (2022) 1382–1391.
- [24] L. Wang, Y. Liu, Q. Shen, J. Liu, Design and experimental verification of a bolt-clamped piezoelectric actuator based on clamping and driving mechanism, *Mech. Syst. Signal Process.* 146 (2021) art. no. 107065.
- [25] J. Deng, S. Zhang, Y. Li, X. Ma, X. Gao, H. Xie, Y. Liu, Development and experiment evaluation of a compact inchworm piezoelectric actuator using three-jaw type clamping mechanism, *Smart Mater. Struct.* 31 (4) (2022) art. no. 045020.
- [26] Z. Liu, Q. Fu, H. Wang, Z. Yao, Z. Dong, L. Zhang, A novel compact bolted-type piezoelectric actuator excited by two excitation methods: design, simulation, and experimental investigation, *Smart Mater. Struct.* 32 (5) (2023) art. no. 055006.
- [27] X. Gao, S. Zhang, J. Deng, Y. Liu, Development of a small two-dimensional robotic spherical joint using a bonded-type piezoelectric actuator, *IEEE Trans. Ind. Electron.* 68 (1) (2021) 724–733.
- [28] Y. Liu, X. Yang, W. Chen, D. Xu, A bonded-type piezoelectric actuator using the first and second bending vibration modes, *IEEE Trans. Ind. Electron.* 63 (3) (2016) 1676–1683.
- [29] Z. Pan, L. Wang, Y. Yang, J. Jin, J. Qiu, A novel bonded-type 3-degree-of-freedom ultrasonic motor: design, simulation, and experimental investigation, *Smart Mater. Struct.* 32 (6) (2023) art. no. 065010.
- [30] X. Tian, Y. Liu, J. Deng, L. Wang, W. Chen, A review on piezoelectric ultrasonic motors for the past decade: classification, operating principle, performance, and future work perspectives, *Sens. Actuators A* 306 (2020) art. no. 111971.
- [31] J. Liu, J. Wu, X. Gao, Z. Ding, W. Wei, Enhancement of torque density and power density of polymer-based ultrasonic motors via flexible usage of anisotropy in elastic property, *Smart Mater. Struct.* 32 (7) (2023) art. no. 075020.
- [32] J. Wu, Y. Mizuno, K. Nakamura, Piezoelectric motor utilizing an alumina/PZT transducer, *IEEE Trans. Ind. Electron.* 67 (8) (2020) 6762–6772.
- [33] S. Dong, S. Wang, W. Shen, L. Li, A miniature piezoelectric ultrasonic motor based on circular bending vibration mode, *IEEE/ASME Trans. Mechatron.* 5 (4) (2000) 325–330.
- [34] H. Li, X. Tian, Z. Shen, K. Li, Y. Liu, A low-speed linear stage based on vibration trajectory control of a bending hybrid piezoelectric ultrasonic motor, *Mech. Syst. Signal Process.* 132 (2019) 523–534.
- [35] J. Yan, Y. Liu, J. Liu, D. Xu, W. Chen, The design and experiment of a novel ultrasonic motor based on the combination of bending modes, *Ultrasonics* 71 (2016) 205–210.
- [36] X. Yang, Y. Liu, W. Chen, J. Liu, Miniaturization of a longitudinal-bending hybrid linear ultrasonic motor, *Ceram. Int.* 41 (2015) 607–611.
- [37] Y. Shi, C. Zhao, A new standing-wave-type linear ultrasonic motor based on in-plane modes, *Ultrasonics* 51 (4) (2011) 397–404.
- [38] J. Wu, L. Wu, R. Song, J. Niu, M. Xie, M. Cao, Q. Zhang, Y. Liu, Y. Li, A two-DOF linear ultrasonic motor with high thrust force density and high power density utilizing torsional/centrosymmetric-bending/symmetric-bending modes, *IEEE Trans. Ind. Electron.* 69 (8) (2022) 8220–8230.
- [39] Q. Wang, X. Du, B. Xu, L.E. Cross, “lectromechanical coupling and output efficiency of piezoelectric bending actuators, *IEEE Trans. Ultrason. Ferroelectr. Freq. Control* 46 (3) (1999) 638–646.
- [40] Y. Liu, W. Chen, X. Yang, J. Liu, A T-shape linear piezoelectric motor with single foot, *Ultrasonics* 56 (2015) 551–556.
- [41] H. Sanikhani, J. Akbari, Design and analysis of an elliptical-shaped linear ultrasonic motor, *Sens. Actuators A* 278 (2018) 67–77.
- [42] L. Wang, X. Li, J. Wu, Z. Ding, F. Du, X. Rong, R. Song, Y. Li, A millipede-inspired miniature self-moving ultrasonic actuator with high carrying capability and nanometer resolution, *Int. J. Mech. Sci.* 267 (2024) art. no. 109017.
- [43] Y. Wang, Y. Cai, H. Gong, Y.-S. Lee, Design and 3D printing of waveguide-based ultrasonic longitudinal-torsional transducers for medical needle insertion, *Sens. Actuators A* 344 (2022) art. no.113706.
- [44] R. Wang, L. Wang, J. Jin, B. Jia, Q. Zhang, D. Wu, Excitation method and electromechanical coupling dynamic model of a novel torsional piezoelectric actuator, *Mech. Syst. Signal Process.* 154 (2021) art. no. 107587.
- [45] J. Niu, J. Wu, M. Cao, L. Wu, A traveling-wave linear ultrasonic motor driven by two torsional vibrations: design, fabrication, and performance evaluation, *IEEE Access* 8 (2020) 122554–122564.
- [46] J. Wu, Y. Mizuno, K. Nakamura, A rotary ultrasonic motor operating in torsional/bending modes with high torque density and high power density, *IEEE Trans. Ind. Electron.* 68 (7) (2021) 6109–6120.
- [47] G.L. Smith, R.Q. Rudy, R.G. Polcawich, D.L. Devoe, Integrated thin-film piezoelectric traveling wave ultrasonic motors, *Sens. Actuators A* 188 (2012) 305–311.
- [48] J. Wu, J. Niu, Y. Liu, X. Rong, R. Song, H. Dong, J. Zhao, Y. Li, Development of a self-moving ultrasonic actuator with high carrying/towing capability driven by longitudinal traveling wave, *IEEE/ASME Trans. Mechatron.* 28 (1) (2023) 267–279.
- [49] K. Smyth, S.G. Kim, Experiment and simulation validated analytical equivalent circuit model for piezoelectric micromachined ultrasonic transducers, *IEEE Trans. Ultrason., Ferroelectr., Freq. Control* 62 (4) (2015) 744–765.
- [50] S.A. Morris, C.G. Hutchens, Implementation of Mason’s model on circuit analysis programs, *IEEE Trans. Ultrason., Ferroelectr., Freq. Control* 33 (3) (1986) 295–298.
- [51] S. Lin, Electro-mechanical equivalent circuit of a piezoelectric ceramic thin circular ring in radial vibration, *Sens. Actuators A* 134 (2007) 505–512.
- [52] V. Ferrari, D. Marioli, A. Taroni, Theory, modeling and characterization of PZT-on-alumina resonant piezo-layers as acoustic-wave mass sensors, *Sens. Actuators A* 92 (2001) 182–190.
- [53] J. Southin, S. Wilson, D. Schmitt, R. Whatmore, $e_{31,f}$ determination for PZT films using a conventional ‘ d_{33} ’ meter, *J. Phys. D Appl. Phys.* 34 (2001) 1456–1460.
- [54] Z. Li, Z. Wang, P. Guo, L. Zhao, Q. Wang, A ball-type multi-DOF ultrasonic motor with three embedded traveling wave stators, *Sens. Actuators A* 313 (2020) art. no. 112161.
- [55] Z. Ding, W. Wei, K. Wang, Y. Liu, An ultrasonic motor using a carbon-fiber-reinforced/poly-phenylene-sulfide-based vibrator with bending/longitudinal modes, *Micromachines* 13 (4) (2022) art. no. 4.
- [56] H. Li, J. Deng, S. Zhang, H. Yu, Y. Liu, Design and experiment of a three-feet linear ultrasonic motor using third bending hybrid modes, *Sens. Actuators A* 331 (2021) art. no. 112990.
- [57] Y. Liu, S. Shi, J. Yan, W. Chen, D. Xu, A novel piezoelectric actuator with two operating modes, *J. Intel. Mater. Syst. Str.* 29 (2017) 1157–1164.



Jinshuo Liu was born in Shandong, China, in 2001. He received his bachelor degree in control science and technology from Shandong University, Jinan, China, in 2024, and will pursue his master degree in control science and technology from Shandong University. His research interests locate in piezoelectric actuation and its application to precise manipulation/operation.



Longhui Ding was born in Henan, China, in 1989. He received the B.E. degree in engineering mechanics from North China University of Water Resources and Electric Power, Zhengzhou, China, in 2013, the M.E. degree in engineering mechanics from Dalian University of Technology, Dalian, China, in 2016. He is currently a structural simulation engineer with Goertek, Qingdao, China, where he is active in structural mechanics simulation and vibration noise control.



Chengqi Pan was born in Jiangsu, China, in 2001. He received the B.E. degree in mechanical engineering from Henan University of Science and Technology, Luoyang, China, in 2023, and is pursuing his master degree in mechanical engineering from Shandong University. His research interests lie in ultrasonic-levitation-based device.



Xuhui Jing was born in Shandong, China, in 1992. He received the B.E. degree in mechanical design, manufacturing and automation engineering from Qingdao College, Qingdao University of Technology, Qingdao, China, in 2015. He is currently employed at Goertek, Qingdao, China, where he is active in the field of active haptics.



Xiaohang Lai was born in Shandong, China, in 2003. He is currently an undergraduate student in School of Control Science and Technology, Shandong University, Jinan, China. His research interest lies in piezoelectric actuation.



Yili Wang was born in Shandong, China, in 1991. He received the B.E. degree in electrical engineering and automation from University of Jinan, Jinan, China, in 2015. He is currently working in Goertek, Qingdao, China, as hardware engineer, dedicated to the hardware development of smart devices.



Jiang Wu was born in Liaoning, China. He received the B.E. degree in mechanical engineering from Dalian University of Technology, Dalian, China, in 2010, the M.E. degree in mechatronic engineering from the State Key Laboratory of Robotics and System, Harbin Institute of Technology, Harbin, China, in 2012, and the Dr. Eng. degree in electric and electronic engineering from the Future Interdisciplinary Research of Science and Technology, Tokyo Institute of Technology, Yokohama, Japan, in 2017. Then, he worked in Tokyo Institute of Technology as a Research Fellow of the Japan Society for the Promotion of Science (JSPS). He is currently a professor with School of Control Science and Technology, Shandong University, where he is active in developing new types of ultrasonically levitating devices and piezoelectric actuators/robots.



Xiaojia Zhu was born in Jilin, China, in 1990. She received the B.E. degree in computer science and technology from Ocean University of China, Qingdao, China, in 2012, the M.E. degree in computer technology from Ocean University of China, Qingdao, China, in 2014. She is currently working as a software engineer in Goertek, Qingdao, China, where she is active in automotive software research and development.



Zhaochun Ding was born in Shandong, China, in 2001. He received his bachelor degree in mechanical engineering from Shandong University, Jinan, China, in 2023, and is pursuing his master degree in control science and technology from Shandong University. His research interests locate in piezoelectric actuation and its application to miniature robots.



Leilei Lv was born in Shandong, China, in 1989. She received the B.E. degree in electronic information science and technology from Chizhou University, Chizhou, China, in 2013. She is currently employed at Goertek, Qingdao, China, where she is active in the field of active haptics.



Lipeng Wang received his B.S. and M. S. degrees in mechanical engineering from Yanshan University, Qinhuangdao, China, in 2018 and 2022, respectively. He is currently a Ph.D. candidate in School of Control Science and Technology, Shandong University, Jinan, China. His research interests include ultrasonic levitation-based devices and piezoelectric actuation.



Xiaoming Yue was born in Hebei, China, in 1988. He received the B.E. degree in mechanical engineering from Nanjing Agricultural University, Nanjing, China, in 2011, the M.E. degree in material processing engineering, Luoyang Ship Material Research Institute, Luoyang, China, in 2014, and the Dr. Eng. degree in mechanical engineering, Harbin Institute of Technology, Harbin, China, in 2018. He is currently an associate professor with School of Mechanical Engineering, Shandong University, Jinan, China, where he is active in developing electromechanical control system.